Detection and Characterization of Natural and Induced Fractures for the Development of Enhanced Geothermal Systems

Final Report

Professor M. Nafi Toksöz
Earth Resources Laboratory
Department of Earth, Atmospheric and Planetary Sciences
54-614
Massachusetts Institute of Technology
Cambridge, MA 02139
Tel 617-253-7852/FAX 617-258-0231 toksoz@mit.edu

April 6, 2013

Abstract

The objective of this 3-year project is to use various geophysical methods for reservoir and fracture characterization. The targeted field is the Cove Fort-Sulphurdale Geothermal Field in Utah operated by ENEL North America (ENA).

Our effort has been focused on 1) understanding the regional and local geological settings around the geothermal field; 2) collecting and assembling various geophysical data sets including heat flow, gravity, magnetotelluric (MT) and seismic surface and body wave data; 3) installing the local temporary seismic network around the geothermal site; 4) imaging the regional and local seismic velocity structure around the geothermal field using seismic travel time tomography; and (5) determining the fracture direction using the shear-wave splitting analysis and focal mechanism analysis.

Various geophysical data sets indicate that beneath the Cove Fort-Sulphurdale Geothermal Field, there is a strong anomaly of low seismic velocity, low gravity, high heat flow and high electrical conductivity. These suggest that there is a heat source in the crust beneath the geothermal field. The high-temperature body is on average 150 ˚C – 200 ˚C hotter than the surrounding rock. The local seismic velocity and attenuation tomography gives a detailed velocity and attenuation model around the geothermal site, which shows that the major geothermal development target is a high velocity body near surface, composed mainly of monzonite. The major fracture direction points to NNE. The detailed velocity model along with the fracture direction will be helpful for guiding the geothermal development in the Cove Fort area.

Introduction

The successful development of Enhanced Geothermal Energy Systems depends critically on the ability to find and characterize the rock, stress field, and fracture system within the geothermal reservoir before, during, and after activities that are designed to improve the productivity of the reservoir. Using the information about the reservoir obtained from geological and geophysical characterization of the existing reservoir can be used to design a viable stimulation plan to enhance the flow and productivity from a geothermal reservoir. Data collected during and after the stimulation must be reliably analyzed to determine the changes the stimulation induced within the reservoir. While the ability to characterize a fracture system and *in situ* stress and flow regimes are of critical importance to both the petroleum and geothermal industries, they remain among the most challenging problems faced in reservoir development. Geothermal systems present some problems not encountered in petroleum development due to the high temperatures of the reservoirs, the presence of steam and water in the pores, and the relatively lower budgets that can be invested to develop a geothermal reservoir compared to petroleum bearing reservoirs.

Fractures are detectable by remote means due to their effects on geophysical properties. For example, the high compressibility of fractures and their complex geometry give rise to strongly anisotropic and spatially heterogeneous seismic velocities. Many of the same aspects of geometry that control the geophysical responses also control the fluid permeability. For this reason, we strive to develop methods that invert the geophysical response for the underlying fracture geometry, in order to predict fluid flow.

This is a three-year project that started on October 1, 2008. In the first year of the project, we focused our effort on understanding the regional and local geology around the Cove Fort geothermal field, and collecting relevant geophysical data and generating initial tomographic models. The geothermal field is located in the transition zone between the Basin and Range to the west and the Colorado Plateau to the east. We collected various geophysical data for the Utah area, including heat flow, gravity, MT, seismic surface wave phase and group velocity maps, seismic body wave travel time data, and full seismic waveforms. Different geophysical data sets have different strengths on characterizing subsurface structures and properties. Combining these data through a coordinated analysis, and when possible, by joint inversion provides a detailed model of the Cove Fort Geothermal region. In the second year of the project, we focused on developing a 10-station seismic network around the Cove Fort to collect local seismic events. In the 3rd year of the project, we focused on analyzing local seismic data using various seismic methods.

Research Accomplished

1. Regional and local geology characterization around the geothermal field

(1) Regional Geology

The Cove Fort-Sulphurdale KGRA (Known Geothermal Resource Area), located in central-western Utah, is characterized by several unique geologic features (Figure 1). To the west lies the expansive Basin and Range Province, with extensional tectonics and a series of normal and listric faults. As a result of the extension, the crust is relatively thin, between 25 and 30 km (Benz et al., 1990). To the east and south of Cove Fort lies the Colorado Plateau, a region of highly elevated sedimentary rocks that are Paleozoic to Mesozoic in age (Figure 2). The striking feature of the Colorado Plateau is its dearth of faulting and deformation.

Figure 1. Google Earth image showing the location of the Cove Fort region.

The Cove Fort-Sulphurdale KGRA itself is located in the transition zone between the Basin and Range Province and the Colorado Plateau (Figure 2). In Utah this transition zone is roughly correlative with the Intermountain Seismic Belt. The Cove Fort geothermal geothermal field is at the convergence of the Tushar Mountains and the Pavant Range, two mountain ranges in this transition zone. Extensive faulting, fractures and hydrothermal activity at other thermal springs in the state are also located in or around the transition zone. Figure 2 shows the location of Utah's known geothermal resources, including the Cove Fort KGRA, as well as the major physiographic regions of the state.

Figure 2. Map showing the major physiographic regions of Utah and the state's geothermal resources. Note that most of the thermal springs are located in or near the transition zone. (From Utah Geological Survey)

(2) Geology of the Cove Fort-Sulphurdale KGRA

Sedimentary rocks forming the basement in the Cove Fort region consist mostly of dolomite, limestone and redbeds (Moore and Samberg, 1979). These rocks are Paleozoic to Mesozoic in age (Ross and Moore, 1985) and were metamorphosed during the Late Cretaceous Sevier Orogeny as the Sierra Nevadas collided with the these rocks (Wannamaker et al., 2008). This resulted in north-trending folds and thrusts throughout the transition zone (Crosby, 1959; Armstrong, 1958). After a period of erosion, these metasedimentary rocks were overlain by the Price River Conglomerate, a Late Mesozoic conglomerate interbedded with sandstone and claystone (Ross et al., 1982).

Tertiary volcanic rocks, deposited between 30 and 19 million years ago, lie stratigraphically above the Price River Conglomerate. Geochemical data suggest that the sources for these rocks are the Basin and Range Province to the west of Cove Fort and the Marysvale Volcanic Field to the east and south (Steven and Cunningham, 1979). The older units in this volcanic sequence, such as the widespread Dog Valley Volcanics, Needles Range Formation and the Three Creeks Tuff Member of the Bullion Canyon Volcanics are predominantly Oligocene in age and consist primarily of lava flows, local and regional phenocryst-rich ash-flow tuffs and breccias (Fleck et al., 1975; Steven et al., 1979). Younger Oligocene to Miocene-aged volcanics in the sequence include tuffs and rhyolitic lava flows (Steven and Morris, 1983). Figure 3 shows a simplified geologic map of the region.

Figure 3. Simplified geological map of the region. Modified from Ross and Moore (1985).

Figure 4. Simplified geologic cross-section of the guide blocks and Tertiary pluton (modified from Ross and Moore, 1985). See Figure 3 for description of units.

Metamorphism and secondary mineralization of the lower Tertiary volcanics and the underlying sedimentary rocks occurred during the emplacement of a hypabyssal pluton of quartz monzonite approximately 27 to 22 million years ago (Moore and Samberg, 1979). While this intrusion lacks a surface expression, several latite porphyry dikes exposed in the northern Tushar Mountains, as well as monzonite dikes intersected during the drilling of CFSU 42-7 suggest that this body has a large subsurficial extent (Ross and Moore, 1985). Figure 4 shows a cross section A to A' (map view shown in Figure 3) that gives one interpretation of the pluton's structure.

The youngest rocks in the region occur to the west of the Cove Fort-Sulphurdale KGRA in the Cove Fort Basalt Field. Quaternary volcanic activity between 1 and 0.3 Ma (Best et al., 1980) produced a shield volcano in this region. At the top of this volcano, called "Burnt Mountain," lies a cinder cone, the vent for most of the basaltic andesites that currently make up the Cove Fort Basalt Field (Steven and Morris, 1983). Some have hypothesized that this basaltic volcanism is the heat source for the current geothermal system at Cove Fort (Callaghan, 1973; Steven et al., 1979).

Hydrothermal alteration in the region is confined to several small locations. The alteration is mostly acid alteration, with some mineralization of galena, flourite, sulphur, gypsum, pyrite and chalcopyrite (Ross and Moore, 1985). Some sulphur deposits also occur along the scarps of the normal faults in the region. In total, there are approximately 47 km^2 of surficial hydrothermal alterations associated with the active geothermal system, the largest concentration of which is located east-southeast of Sulphurdale (Ross and Moore, 1985). The black patches in the geologic map of the region (Figure 3) show where many of these alteration areas are located.

Extensional stresses due to Basin and Range tectonics control the major structures in the Cove Fort-Sulphurdale region. Normal faults near the Pavant Range-Tushar Mountains junction are due to this extension and are believed to have first faulted approximately 7 Ma (Rowley et al., 1979). The scarps of these faults, with the exception of the E-W trending Cove Creek Fault, are mostly high-angle northerly and north-easterly trending normal faults and low-angle westerly-dipping listric faults (Steven and Morris, 1983). The gravitational glide blocks associated with the low-angle faulting may provide the impermeable caps to the geothermal reservoir (Ross and Moore, 1985). Figure 5 provides a representation of the regional structural

geology. From this model, it is easy to see how the geometry of the faults plays a major role in the distribution of geothermal fluids.

Figure 5. Schematic model of the Cove Fort-Sulphurdale geothermal resource showing the structural relationship between high-temperature fluids in faults and the previously known moderate-temperature reservoir. The black arrows depict thermal brine upwelling, white arrows show movement of groundwater and hatched arrows represent the fluid movement of mixed ground and thermal waters. (Ross and Moore, 1985)

2. Assembling Geophysical Data in Utah

(1) Surface Heat Flow in Utah

Heat flow is a quantity defined by the amount of thermal energy passing through a given area of rock in a given amount of time. Since heat flow is primarily toward the earth's surface, it is generally modeled one dimension with the expression: $q = -k (dT/dz)$, where q is the surface heat flow, measured in $m\text{Wm}^{-2}$, k is the thermal conductivity in $\text{Wm}^{-1}\text{K}^{-1}$ and dT/dz is the vertical geothermal gradient (Haenel et al., 1988). In the state of Utah, several studies have attempted to quantify the surface heat flow using this relationship. Most recently, Henrikson and Chapman (2002) determined heat flow in 88 oil and gas wells around the state using temperature probes to gather gradient data and lithological well logs to estimate conductivity values. Their data, as well as data from hundreds of other sites across the state are compiled in Southern Methodist University's Geothermal Database run by David Blackwell and Maria Richards.

Over 900 sites in Utah with thermal gradient and heat flow values are listed in the database, with values from Henrikson and Chapman (2002) and several other sources. Using these values, we used ArcGIS to create interpolated gradient and heat flow maps for the state. Figure 6 shows the wells with measured thermal gradient values and the results of the interpolation. Values range from about zero to over 500 ºC/km, with the highest thermal gradients occurring at Cove Fort and other high areas near the Newcastle Geothermal Area, Crater Springs KGRA and northeast of Salt Lake. Figure 7 is a map showing interpolated values of available heat flow measurements throughout the state. The region with the highest heat flow (over 600 $m\text{Wm}^{-2}$) occurs at Cove Fort and to the east of the KGRA in the Marysvale volcanic area. Northeast of Salt Lake and the Newcastle Geothermal Area are locations where heat flow is also relatively elevated, reaching values of up to 260 $m\text{Wm}^{-2}$.

Figure 6. Interpolated thermal gradient map of Utah. Black dots indicate well locations and the yellow square is the current production well at Cove Fort. Data points from the SMU Geothermal Database.

Figure 7. Interpolated heat flow map of Utah. Black dots indicate well locations and the yellow square is the current production well at Cove Fort. Data points from the SMU Geothermal Database.

(2) Gravity Data

Gravity measurements provide constraints on rock density variations. They are useful for identifying potential geothermal resources. For example, partial melting results in lower rock density and thus is shown as a more negative gravity anomaly. Using gravity observations, we can conduct a three-dimensional gravity inversion to determine the density structure, which has the greater resolving power at shallow depths because gravity anomalies decrease in amplitude and increase in wavelength with increasing depth. Both free-air and Bouguer gravity anomaly data are extracted from the North American Gravity Database managed by the University of Texas at El Paso (Figure 8). The Bouguer gravity anomaly map clearly shows two more positive gravity anomalies, one located in the north central and another located in the southwest of the Utah area. The northern more positive gravity anomaly corresponds to the Great Salt Lake area. The southern high gravity anomaly corresponds to the Washington area. The Cove Fort geothermal area is associated with the more negative gravity anomaly, indicating partial melting or extensive fracturing at depth.

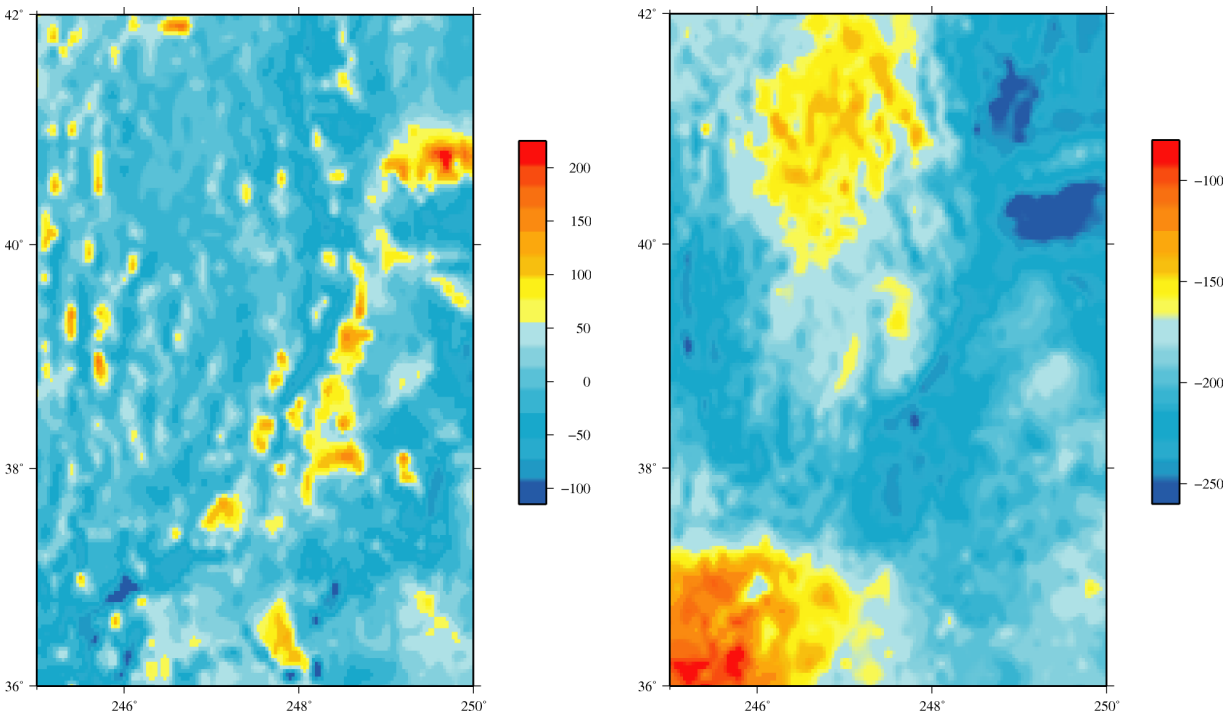

Figure 8. Free-air (left) and Bouguer (right) gravity anomalies of the Utah area. Green box indicates the location of the current production well.

(3) Seismic Surface Wave Data

We have requested surface wave group and phase velocity maps for the Utah area (Figure 9) from the University of Colorado (Yang et al., 2008). Surface wave Green's functions among station pairs are constructed from continuous noise recordings on USArray stations. The dispersion curves are then constructed and used to invert for group and phase velocities at different periods from 8 seconds to 40 seconds. The spatial resolution of the group and phase velocities is 0.5°. Surface wave measurements at shorter periods provide better constraints on the near surface structure. When compared to the Bouguer gravity anomaly map shown in Figure 8, it can be seen that there are consistent features. Generally more negative gravity anomalies correspond to the low velocities and more positive gravity anomalies are associated with high velocities. For example, the more positive gravity anomaly shown in the northern part of the study region corresponds to a high velocity anomaly. The northeast-southwest trending low velocity anomaly is associated with the low gravity anomaly. The Cove Fort - Sulphurdale Geothermal Field is associated with strong, low velocity anomalies.

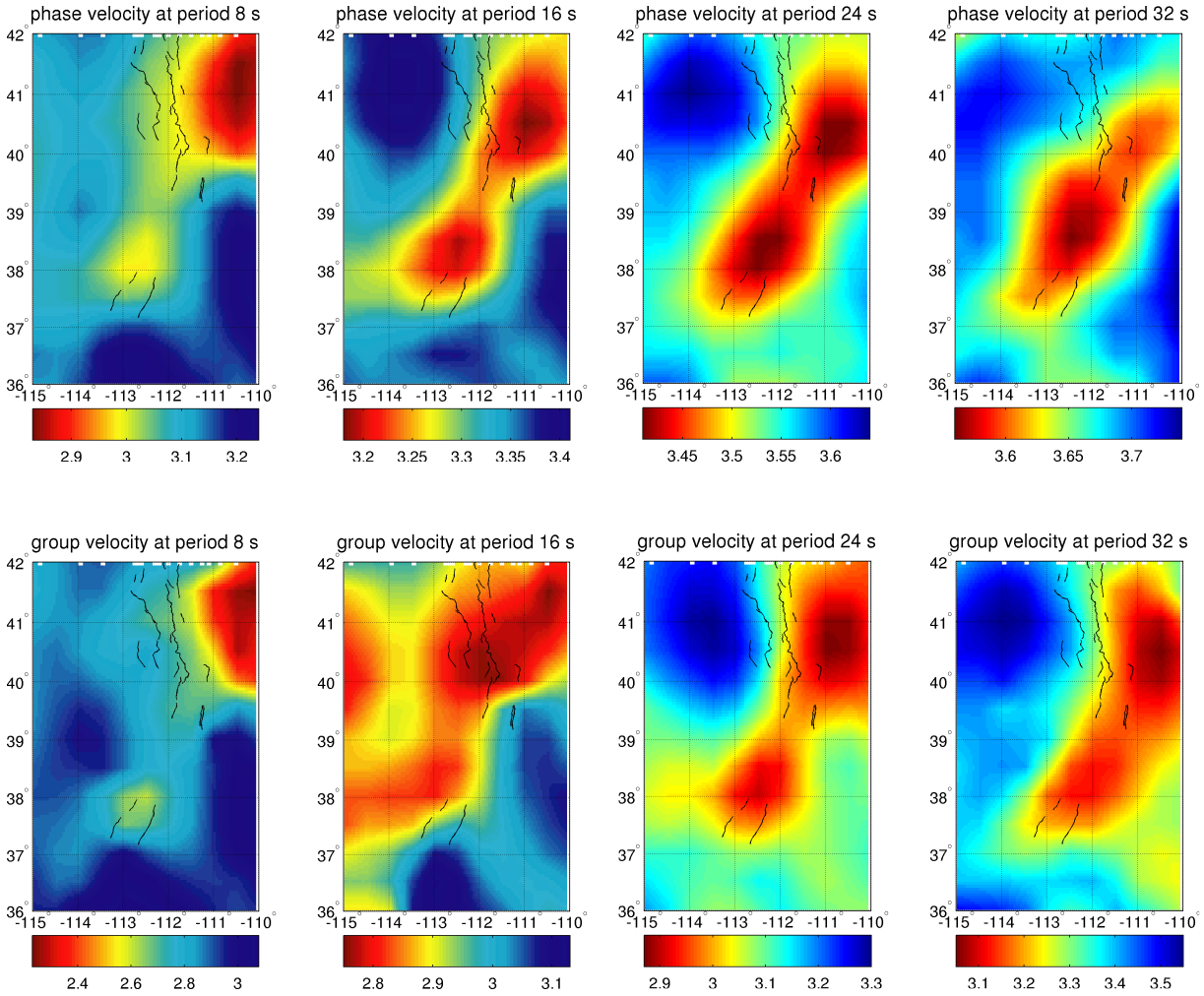

Figure 9. Surface wave phase (top) and group (bottom) velocity maps at periods 8 s, 16 s, 24 s, and 32 s. Green box indicates the location of current production well.

(4) Seismic travel time data

We collected both first P and S arrival time data recorded by the USArray network and University of Utah Seismograph Stations (UUSS) from ~6500 earthquakes. Each event has at least 6 arrivals for reliably determining its location. In addition, we also assembled seismic waveform data from the USArray network and UUSS for future waveform cross-correlation analysis and seismic attenuation tomography. Figure 10 shows the P-wave ray path distribution, as well as the event and station distribution. It shows that the ray distribution is dense near the Cove Fort geothermal area, indicating that we can resolve the fine seismic velocity structure there.

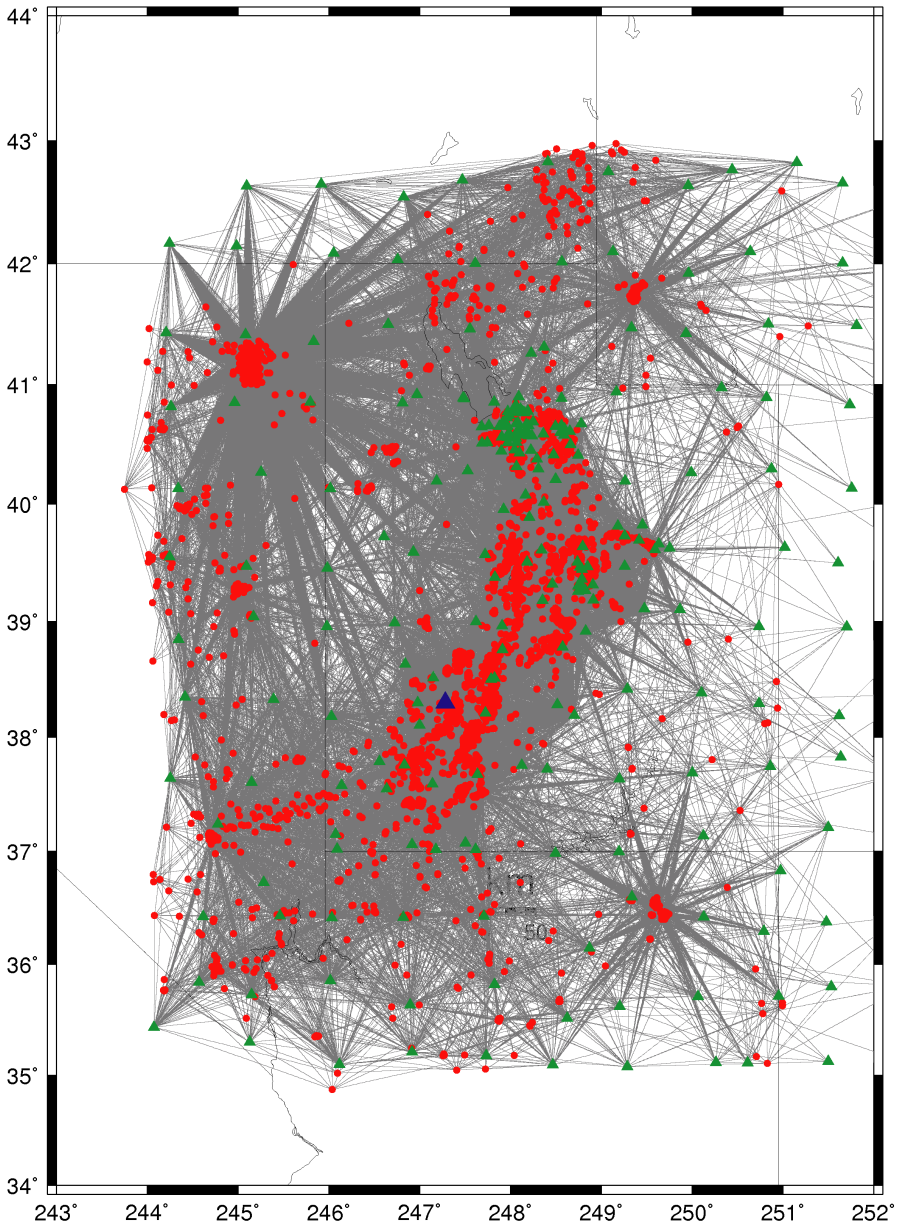

Figure 10. P-wave ray path distribution for the Utah area. Red dots are earthquakes and green triangles are seismic stations. Blue triangle indicates the location of Cove Fort.

(5) Magnetotelluric (MT) Data

We have obtained the 140-station magnetotelluric (MT) and Time Domain Electromagnetic (TDEM) array data that were collected by ENA during November to December, 2007 (Figure 11). The MT data will be used to formulate and constrain the subsurface resistivity structure and, combined with other data (e.g., gradient boreholes), to help infer the temperatures within and below the reservoir.

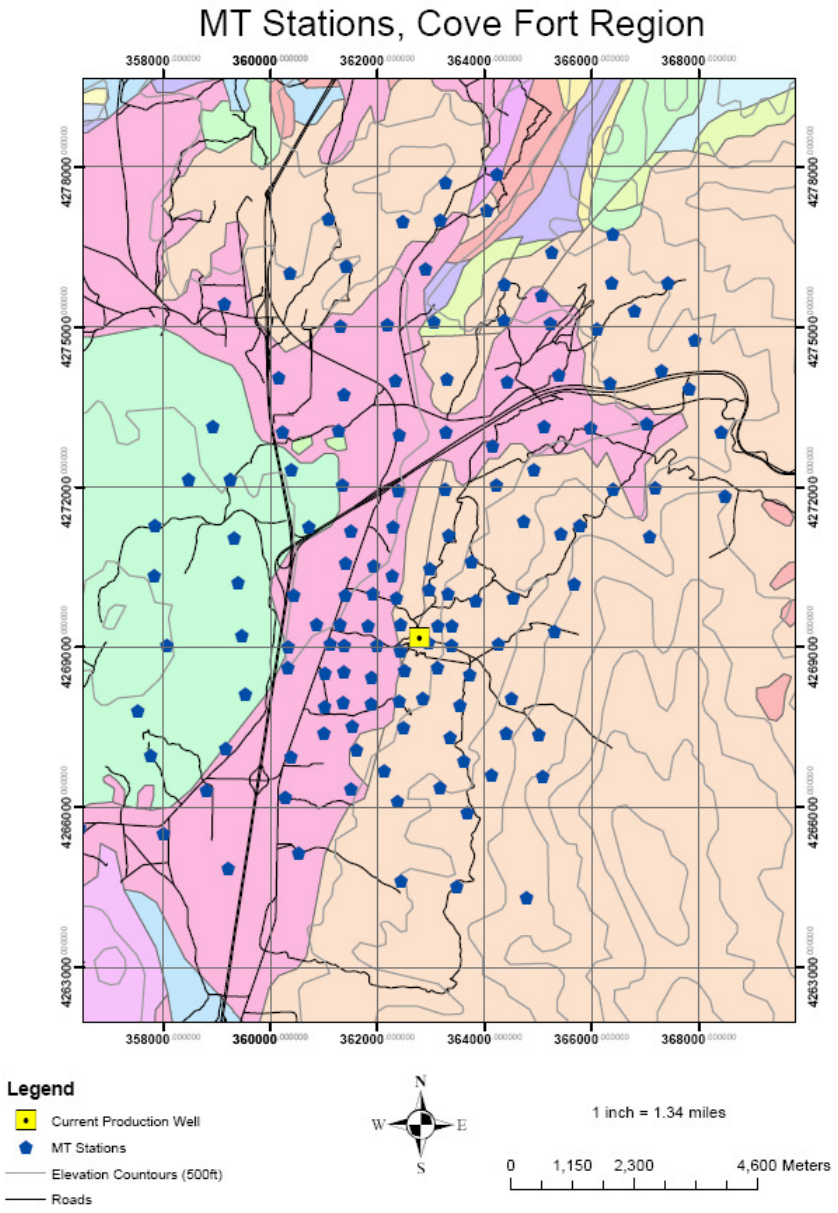

Figure 11. Magnetotelluric Survey conducted by Enel North America, Inc. during November to December, 2007. There are 140 stations in total.

3. Seismic velocity tomography using the double-difference tomography method

We applied the Double-Difference seismic tomography method of Zhang and Thurber (2003) to the measured differential arrival times from waveform cross-correlation analysis. The DD tomography method uses a combination of absolute and more accurate differential arrival times from earthquake pairs observed at common stations and hierarchically determines the velocity structure from larger scale to smaller scale. This method is able to produce more accurate event locations and velocity structure near the source region than standard tomography, which uses only absolute arrival times.

We have obtained the 3D Vp model by applying the regular grid DD tomography code tomoDD to the study region (Figure 13). The inversion grid node spacing in horizontal directions is 0.2° and varies from 3 to 6 km in depth. The inversion starts from the 1D Vp model used by UUSS for routine earthquake locations. The starting root-mean-square (RMS) travel time residuals are 1.58 s for absolute times and 1.72 s for CC times. The final RMS residuals are 100 ms for absolute times and 7 ms for CC times, respectively. Beneath the Cover Fort geothermal area, there is a strong low velocity anomaly at depths from 6 and 24 km, indicating a potential heat source body. We also see low velocity anomalies in some other areas, such as Sanpete located around latitude 39.5° and longitude -111.5°. Figure 14 shows the East-West cross-section of the Vp model at the Cove Fort geothermal area. The low velocity anomaly is evident in the depths down to 20 km.

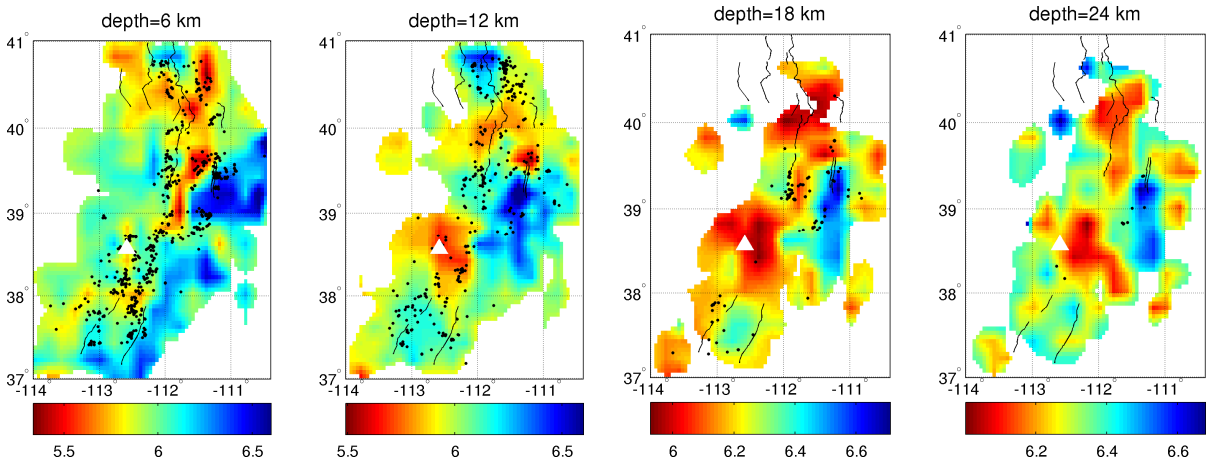

Figure 13. Vp double-difference velocity model at 6km and 12 km. Cove Fort is located at the white triangle.

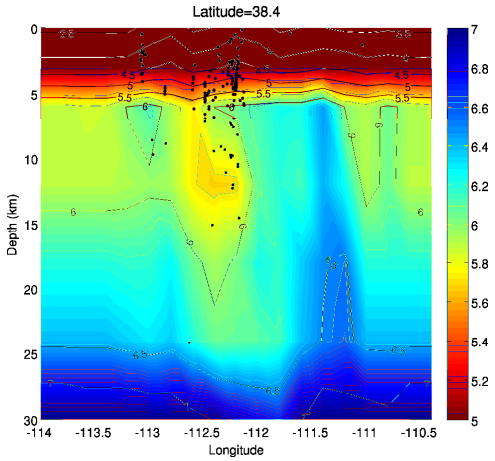

4. Joint inversion of seismic surface wave and gravity data

Surface waves dispersion measurements are primarily sensitive to vertical shear-wave velocity averages. But, at shallow depths, it is difficult to obtain high-resolution velocities and to constrain the structure because short periods are difficult to measure especially in tectonically and geologically complex areas. In comparison, gravity inversions have the greatest resolving power at shallow depths because gravity anomalies decrease in amplitude and increase in wavelength with increasing depth. Gravity measurements also provide constraints on rock density variation. Here we followed the method of Maceria and Ammon (2009) to jointly invert for the 3D Vs model using the seismic surface wave group and phase velocities and gravity anomaly observations. The analytical formmula of Plouff (1976) was used to calculate the 3-D gravity anomalies of a prism with arbitrary dimensions. One point at surface is affected by many prisms and the total gravity anomaly is the sum of anomalies from many prisms.
To jointly invert for surface wave group and phase velocities, one difficulty is to determine a relationship between different physical paramters of density and velocity. Here we used an empirical relationship of Vs and density developed by D.G. Harkrider (personal communication, 2009), shown in Figure 15. For the joint inversion, another difficulty is to determine how to weight two different systems because they have different senstitivities to the model parameters and different data quantity and quality. Here we determine their relative weightings through a trade-off analysis of surface wave residual and gravity data residual (Figure 16). As a result, the resulted model optimally fits both the surface wave and gravity data. In this study, the surface wave is weighted 50 times of the gravity data (1:0.02). Compared to the inversion only using the surface wave data, at shallow depths (e.g., 1 and 5 km), the Vs models better delineate the low velocity anomaly. The 1st-order horizontal and vertical smooth weighting are also applied to constrain the model during the joint inversion. After 3 iterations of joint inversion, the surface wave data residual is close to zero and the gravity data residual decreases ~90%. Figure 17 shows the horizontal slices of the Vs model at depths 1 and 5 km from joint inversion and surface wave inversion only. It shows that the Vs models at shallow depths from joint inversion better delineate the low velocity and better reflects near surface heterogeneities. For the deeper depths, the joint inversion using all three data types including travel time, surface wave and gravity data better defines the low velocity anomaly associated with the transition zone from the Colorado plateau to the Basin and Range (Figure 18).

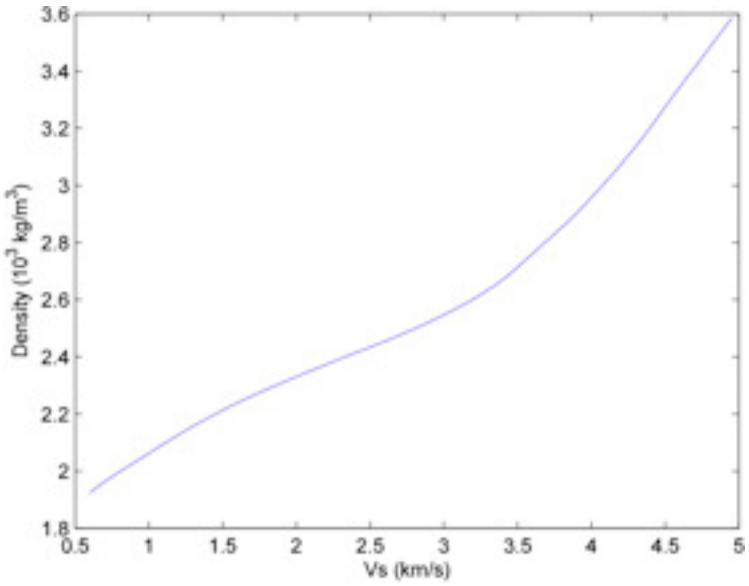

Figure 15. Vs and density relationship

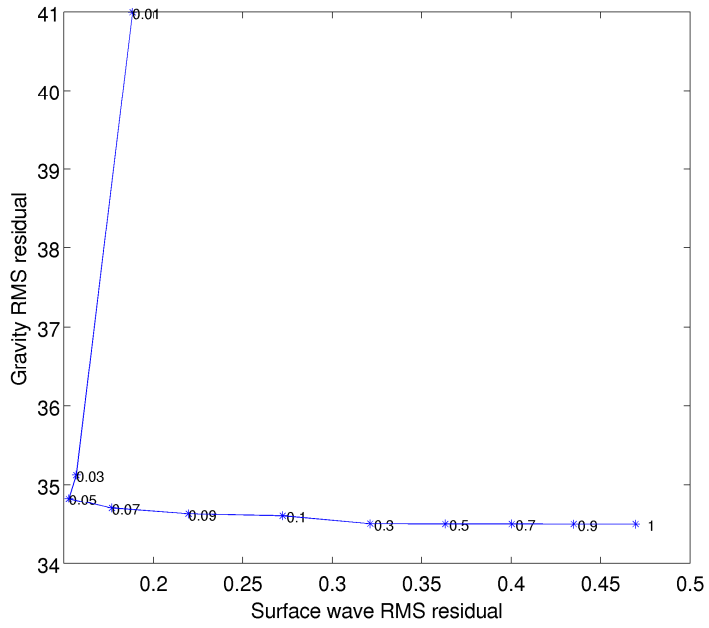

Figure 16. Trade-off curve of surface wave and gravity data residuals for different weightings.

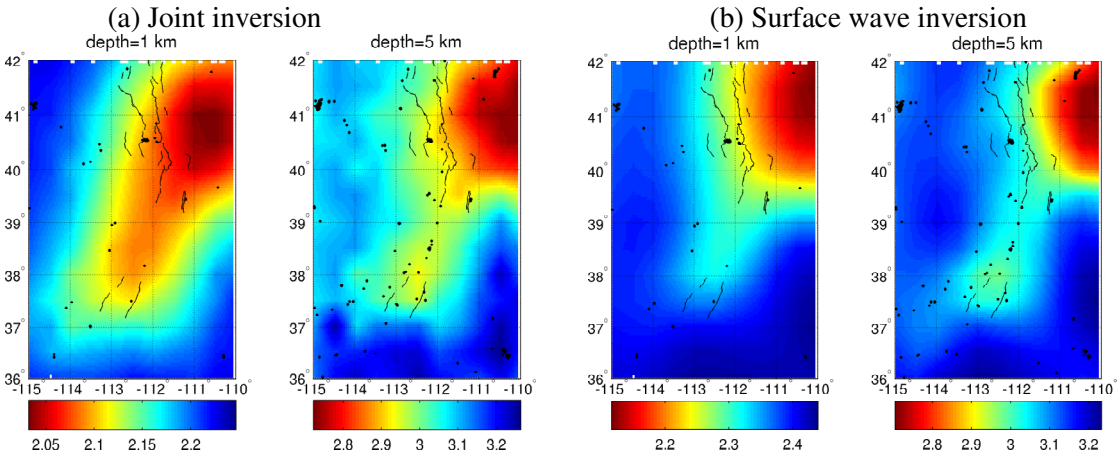

Figure 17. Comparsion of Vs models at shallow depths from joint inversion and surface wave inversion only.

Surface wave **surface+gravity** **surface+body wave** **all three data types**

Figure 18. Comparsion of Vs models at the depth of 30 km from different inversions.

5. Temperature Characterization From the Regional Velocity Model

One of the most important aspects of geothermal energy exploration is temperature characterization. Being able to discern the hottest areas of a geothermal reservoir enables increased thermal energy extraction, resulting in a more economic resource. In order to estimate the subsurface temperature of the geothermal resource at Cove Fort, the Vp velocity model of Toksöz et al. (2010) is used along with laboratory data.

The relationship between temperature and seismic velocity at a certain pressure p is shown through the relationship:

$$\Delta T = \Delta V / (dV/dT)p \qquad \text{(Eq. 1)}$$

At Cove Fort, the 3D Vp model is obtained from the double-difference tomography of regional earthquake travel time data discussed in the previous section. At 3 km, 6 km, 12 km and 18 km,

the average Vp is calculated and the deviation from that value in each 0.1˚ by 0.1˚ grid provides the ΔV values needed for the ΔT calculation. The area used in this study lies between longitudes of -113° W and -112° W and latitudes of 39° N and 38° N.

Values for (dV/dT)p are determined from laboratory data. With the absence of cores from wells at Cove Fort, it is necessary to use laboratory data on other rocks to estimate dV/dT at different pressures. Hughes and Maurette (1956) and Hughes and Maurette (1957) measured the elastic properties of several granites from cores at differing pressures and temperatures. One of these granites, the Woodbury Biotite Granite, is assumed to be similar in composition to the crystalline rocks that underlay Cove Fort. The Woodbury Biotite Granite is composed of 40% quartz and 20-30% microcline with biotite, plagioclase (oligoclase) and muscovite making up the other major minerals. The density of the granite is 2.61 g/cm3. TABLE 1 illustrates the variation between Vp values across temperatures at a range of pressures for the Woodbury Biotite Granite. Although the subsurface lithology at Cove Fort may differ from this assumed composition, the temperature dependence of velocity in other crystalline rocks in the upper crust will be similar to those shown in this table.

TABLE 1. Vp dependence on temperature for the Woodbury Biotite Granite at a range of pressures. Data from Hughes and Maurette (1956) and Hughes and Maurette (1957).

	Vp (km/sec) for increasing pressure						
Temp (˚C)	0.5 kbar	1.0 kbar	1.5 kbar	2.0 kbar	3.0 kbar	4.0 kbar	5.0 kbar
25	6.05	6.16	6.2	6.22	6.26	6.29	6.31
100	6.04	6.13	6.18	6.21	6.22	6.26	6.29
200	6.00	6.06	6.13	6.15	6.18	6.20	6.22
300	5.77	5.87	5.92	5.95	6.01	6.04	6.08

Since the ΔV being used for the temperature calculation is dependent on depth, it is necessary to determine the depth-dependent dV/dT curves. Using the assumption that the rock in the region is of similar composition to the Woodbury Biotite Granite, it is possible to estimate the depths (h) where these pressure-dependent (P) curves are valid using the gravitational constant (g) and the density (ρ) of the granite:

$$P = \rho g h \qquad \text{(Eq. 2)}$$

At 3 km, the pressure is 770 bar, at 6 km, the pressure is 1.5 kbar, at 12 km, the pressure is 3.1 kbar and at 18 km, the pressure is 4.7 kbar. To allow for the smoothest curve possible, we average the Vp vs. T curves at 0.5 and 1 kbar for 3 km; 1, 1.5 and 2 kbar for 6 km; 2, 3 and 4 kbar for 12 km; and 4 and 5 kbar for 18 km. To obtain dV/dT, it is necessary to take the derivatives of the curves at the depths of interest. FIGURE 8 displays the best-fit polynomial curves for Vp versus temperature for depths of 3 km, 6 km, 12 km and 18km, averaged from three pressure curves as described in above.

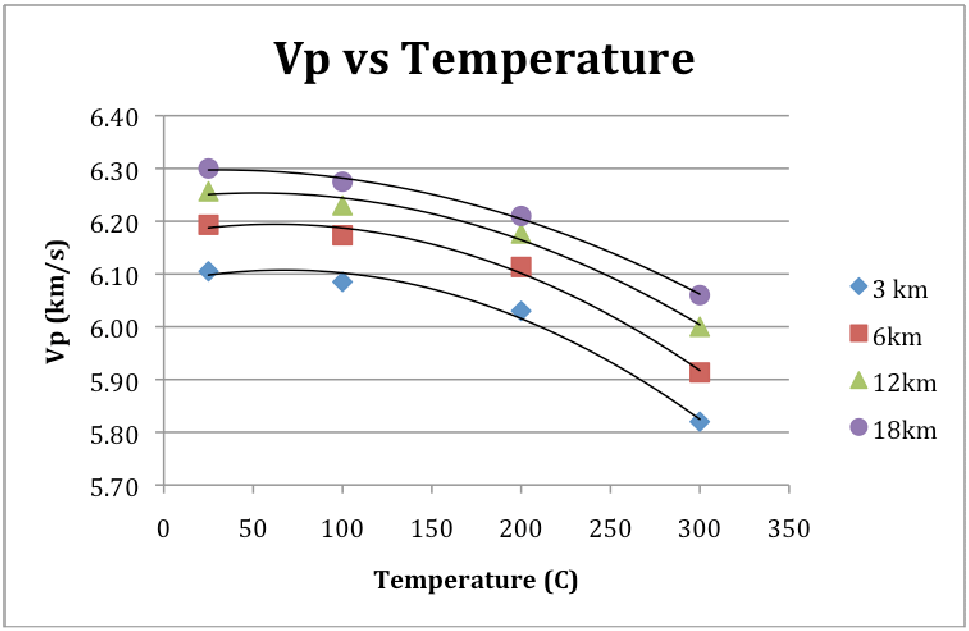

Figure 19. Graph showing the Vp vs T values and their best-fit polynomial curves at 3 km, 6 km, 12 km and 18 km.

With the ΔV known for each 0.1˚ by 0.1˚ at 3 km, 6 km, 12 km and 18 km from seismic tomography and dV/dT at different depths determined from the method outlined above, using EQUATION 1 it is possible to calculate ΔT. However, to obtain absolute values for temperature from ΔT, a background thermal gradient is needed. For this region, a geothermal gradient of 25˚C/km is assumed. Using this assumption, for each grid at each depth, absolute values for temperature are determined.

To obtain a continuous estimation of temperature in this region, a three-dimensional block model similar to Benson (2009) is constructed. Each block in the 3D model is assumed to be homogenous, with constant values for thermal conductivity (a granitic average of 2.85 microWatts/cubic meter), heat capacity (850 J/kg˚C) and density (the density of the Woodbury Biotite Granite, 2.61 g/cm^3). The absolute temperature values for each 0.1˚ by 0.1˚ at 3 km, 6 km, 12 km and 18 km are entered into the model and the vertical boundaries are assumed to be thermally insulated. Then, using the heat flow equation in Comsol Multiphysics, temperature is calculated for each point in the 3D volume.

The results for the heat flow model are shown in Figure 20. Since the Vp model is not entirely accurate at depths less than 3 km, those results are ignored in the interpretation of the model.

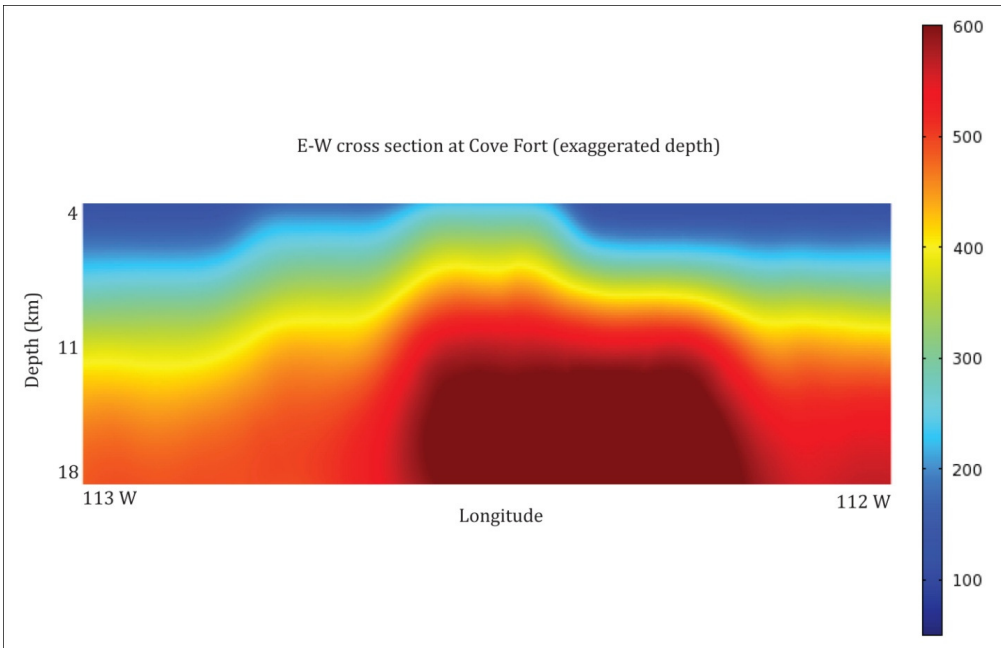

Figure 20. Temperature (in degrees Celsius) along the E-W cross-section at Cove Fort.

The temperatures in the study area show, as expected, elevated temperatures underneath the Cove Fort geothermal field, with values of approximately 250 ˚C at 4 km increasing to above 600 ˚C at 18km. On average, the temperatures in the hot body are 150 ˚C – 200 ˚C greater than the temperatures in the surrounding rocks. The hot body that contains these elevated temperatures appears to shift eastward with depth, a trend consistent with the low velocity body in the Vp model.

There are a few assumptions and drawbacks in this temperature model. First, the temperature values are not accurate at depths shallower than 3 to 4 km. This is because the Vp model used to calculate temperature is a regional velocity model that was focused on constraining deeper velocity anomalies. Second, the region is assumed to have the elastic and thermal properties of the Woodbury Biotite Granite. In reality, the geology is quite complex, displaying a wide variety of rock types, ages and compositions. Another drawback of the model is that it does not take convective heat transfer into account. The ground underneath Cove Fort is very permeable; there are several fractures in the Cove Fort region that act as conduits for abundant geothermal fluids to transfer thermal energy. Therefore, the temperatures modeled, especially at shallow depths, are likely lower than they actually are.

Ignoring the effects of convective heat transfer also explains why the heat flow in this model is lower than measured values. The measured heat flow values around Cove Fort are, on average, about 250 mW/m2, while the modeled heat flow is about 100 mW/m2. However, these measurements were made in wells whose thermal signatures are highly dependent on convective heat transfer, since convecting fluids dominate the geothermal system. The modeled value of approximately 100 mW/m2 around Cove Fort does not take convective heat transfer into account, hence the discrepancy between the values. Still, the heat flow trend is the same for both measured and modeled heat flow. In both instances, the heat flow at Cove Fort is twice the heat flow in the region surrounding the geothermal reservoir.

6. Detailed seismic study around the Cove Fort geothermal site from a local seismic array

(1) 10-station temporary network

We installed 10 seismic stations around the Cove Fort geothermal site (Figure 21). The sensor is broadband seismometer manufactured by Guralp in UK (part model CMG-T3E-0026). Two field trips are arranged for seismic station installation because the difficulty of getting permits for two stations 4 and 5 in August. The first installation occurred from August 15 to August 28, 2010 and 8 stations were installed (sites 1A, 1B, 2, 3, 6, 7, 8, 9 and 10). The second installation occurred between October 3 and 8 of 2010 to install stations 4 and 5 and download seismic data from the first installation. Figure 22 shows a typical seismic station installed for this project. For each station, the seismic sensor is aligned to true North using a magnetic declination of 12.5 degrees. All stations use two 40W solar panels which face roughly south. Solar panel angle is about 38 degrees from the horizontal. 4 people from MIT and 2 people from ENEL North America are involved in the installation. The network operated for about 1 year and we used the well known seismic analysis software Antelope to detect about 500 seismic events (Figure 21). Figure 22 shows a typical waveform recorded by our seismic network.

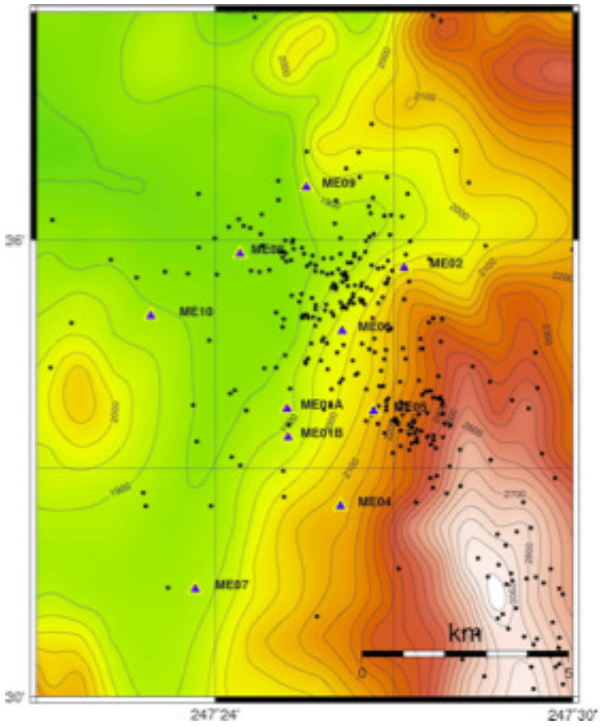

Figure 21. Distribution of seismic stations and events around the Cove Fort geothermal site.

Figure 22. A typical seismic station installed for this project. Two solar panels are used for each station to charge the battery.

Figure 23. Example waveforms from one detected local event. Both first P and S arrivals can be clearly identified.

(2) Analyzing the seismic data collected from the temporary seismic network

We manually picked first P and S arrivals from the waveform data that we collected. We also performed the cross-correlation analysis to determine the accurate differential arrival times from event pairs to common stations using the package called BCSEIS. Generally the cross-correlation delay times are calculated using the 2nd order cross-correlation algorithm and are selected only based on cross-correlation coefficients (e.g. >0.7). However, it is difficult to set up an appropriate threshold. If it is too high, many good quality data may be discarded. If it is too low, many unreliable differential times are selected. The cross-correlation package BCSEIS developed by Du et al. (2004) deal with this problem by computing additional estimates of the time delay with the bispectrim (BS) method. The BS method, which works in the third-order spectral domain, can suppress correlated Gaussian or low-skewness noise sources. Du et al. (2004) adopt this method to calculate two additional time delay estimates with both the raw (unfiltered) and band-pass filtered waveforms, and use them to verify (select or reject) the one computed with the CC technique using the filtered waveforms. Thus this BS verification process can reject unreliable CC time delay estimates and also can accept additional CC time delays even if their associated CC coefficients are smaller than a nominal threshold value if they pass the BS verification procedure. We used the double-difference seismic location method to determine locations of 500 events we detected. The new locations are concentrated and show some linear features. (Figure 21)

(3) Determining 3D Vp and Vs models of the Cove Geothermal Site using the double-difference tomography method

It is shown that the earthquakes are distributed mainly in the direction of northwest to southeast (Figure 21). From these 500 earthquakes, we selected about 200 seismic events that are located within the seismic station network for seismic location and tomography (Figure 24). Here we adopted the double-different (DD) seismic tomography method developed by Zhang and Thurber (2003). The DD method has the advantage of using the different arrival times from event pairs to the common stations. The differential times can be calculated by using the waveform cross-correlation times or by subtracting absolute arrival times.

We used the checkerboard resolution analysis method to choose the inversion grid for seismic tomography that is appropriate for the event and station distribution. We also select the optimal regulation parameters such as the smoothing and damping parameters through a careful trade-off analysis. Figure 25 shows the checkerboard recovery patterns for P and S wave models at different depths. It can be seen that the data can resolve the model scale of 1 km down to depth of 2 km. In comparison, the model is resolved worse at the depth of 4 km. With the optimal regularization parameters and the inversion grid, we obtained the P- and S-wave velocity models of the Cove Fort geothermal area (Figure 26). It can be seen that in the middle model region, there exist strong high velocity anomalies.

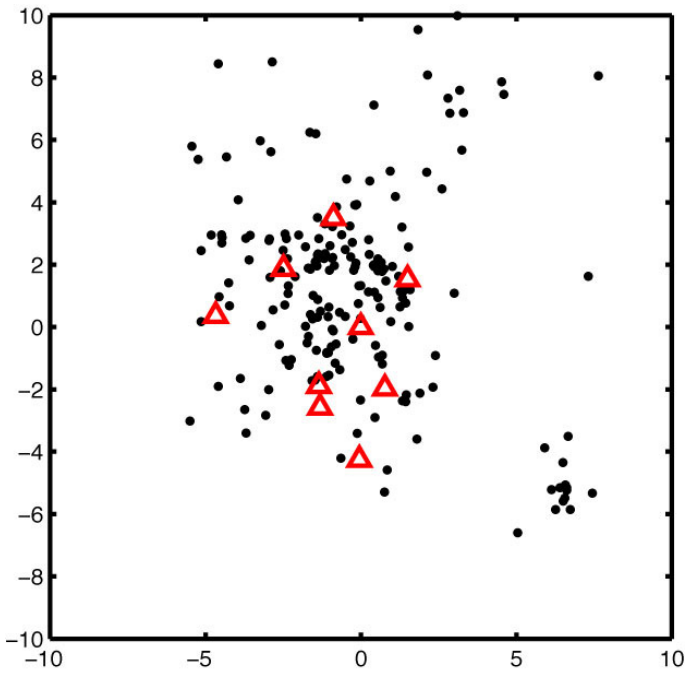

Figure 24. Selected seismic events for double-difference tomography.

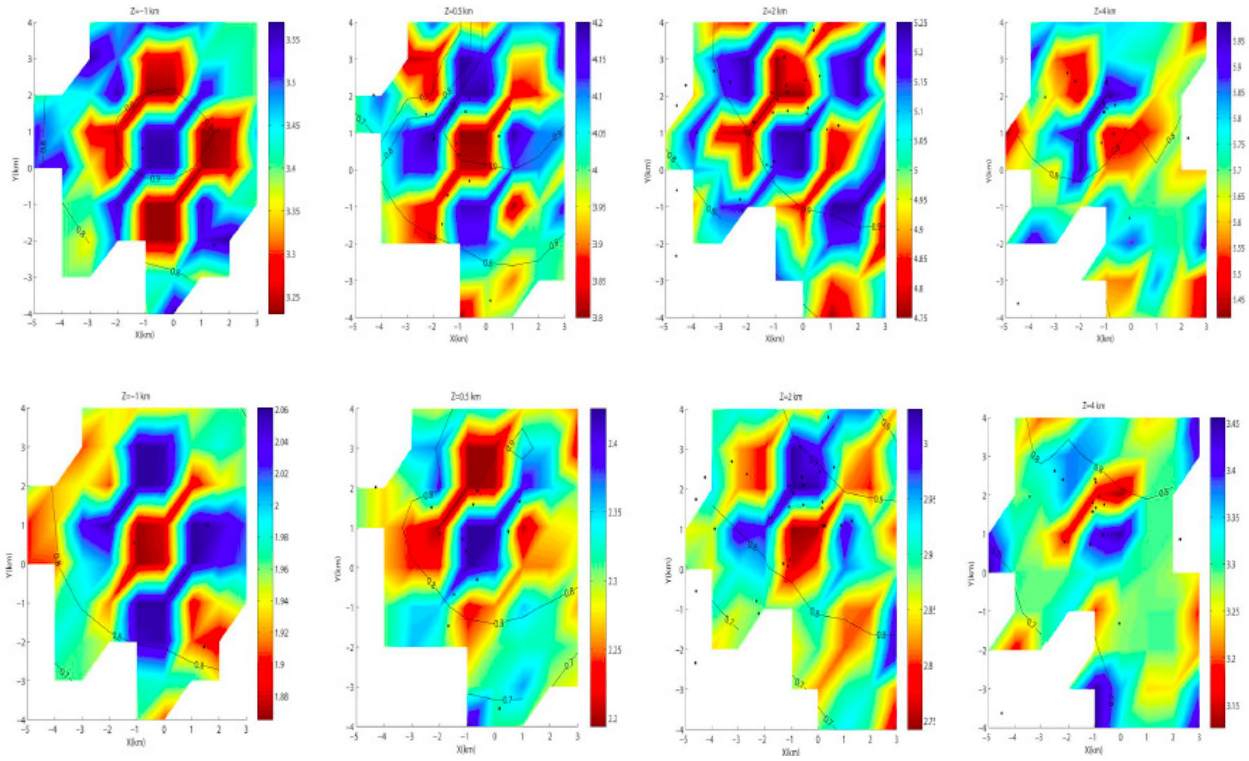

Figure 25. Checkerboard test results for P (top) and S (bottom) velocity models.

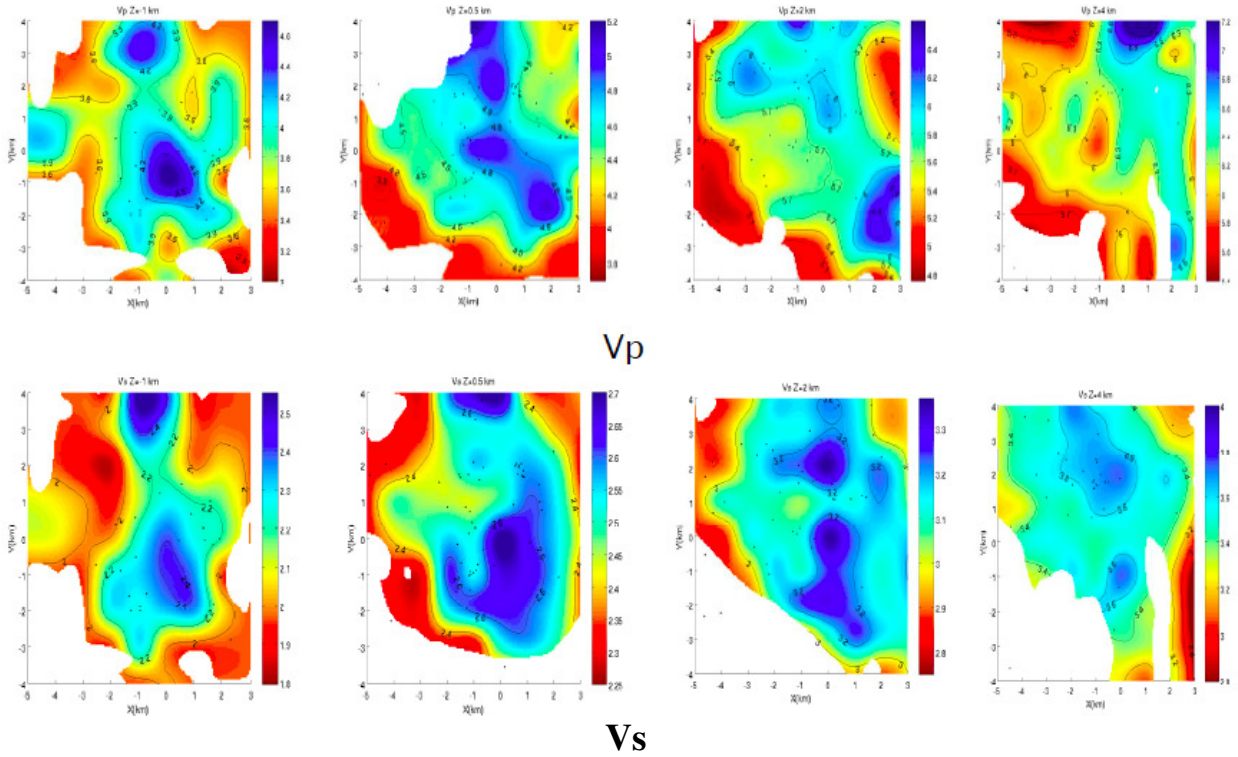

Figure 26. Horizontal slices of the Vp and Vs models at different depths.

(4) Attenuation tomography using the local data

Our approach follows that of Rietbrock (2001) but with the possible addition of a correction for site response following Ponko and Sanders (1994) and Romero et al. (1997). Briefly, the set of spectra for a given event at each of the observing stations j will be fit to an Ω-square source model with a single corner frequency, using

$$\ln(A_j(f)) = \ln(\Omega_{0j}) - \ln(1 + (f/f_c)^2) - \pi f t_j^* \qquad \text{(Eq. 4)}$$

where A_j is the spectral amplitude at frequency f for the event observed at station j, Ω_{0j} is the long-period spectral plateau level, f_c is the corner frequency for the event, and t_j^* is the whole path attenuation operator for the event path to station j (Rietbrock, 2001):

$$t_{ij}^* = \int_{path} \frac{dr}{V_{ij}(r)\, Q_{ij}(r)} \qquad \text{(Eq. 5)}$$

Equation (5) is fit for the range of frequencies with adequate signal-to-noise ratio. The set of all t* values is then inverted for the 3D Q structure, using the 3D seismic velocity model and associated event locations to determine the ray paths for the t* integral. Figure 27 shows the spectrum fitting using equation (4) for one event received at 5 stations. It gives the t* values for each event and station pair as well as the corner frequency.

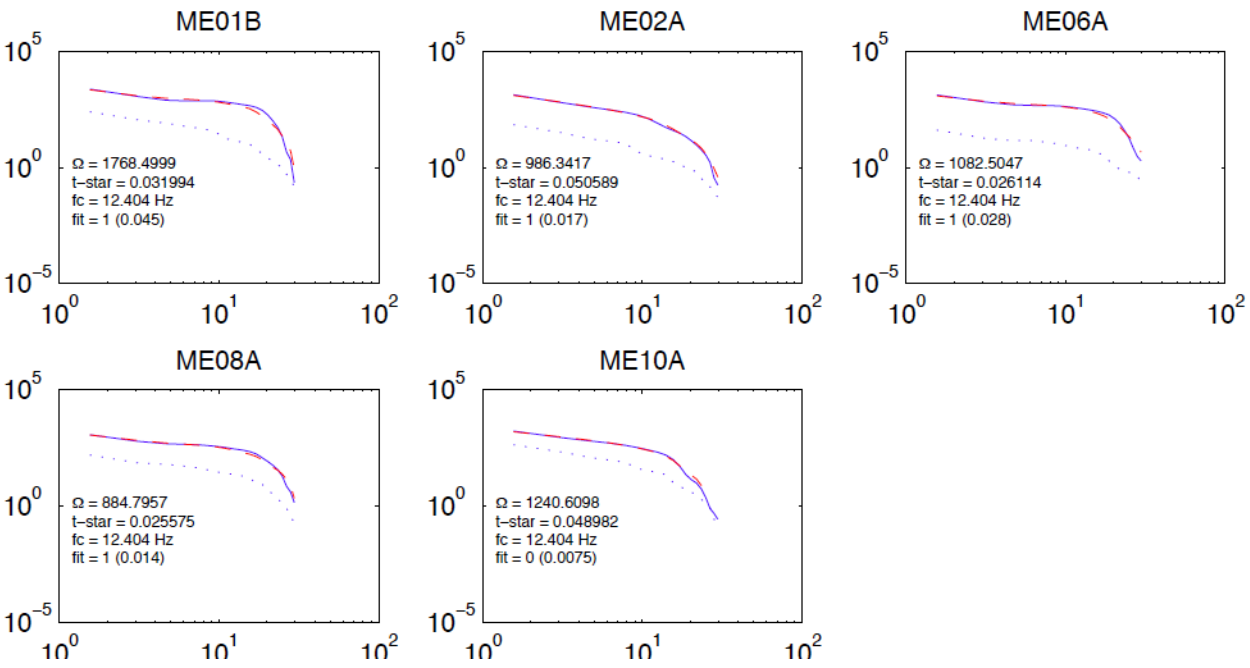

Figure 27. Example of spectrum fitting to find t* values.

Once the velocity and event locations are determined, we can use Eq. 6 to determine the attenuation model Qp (Figure 28). Overall, it shows a trend that in the western part of the study area, the attenuation is stronger. By combining the shear wave splitting results and the attenuation tomography results, the western part may be more suitable for geothermal development where the fractures are more developed.

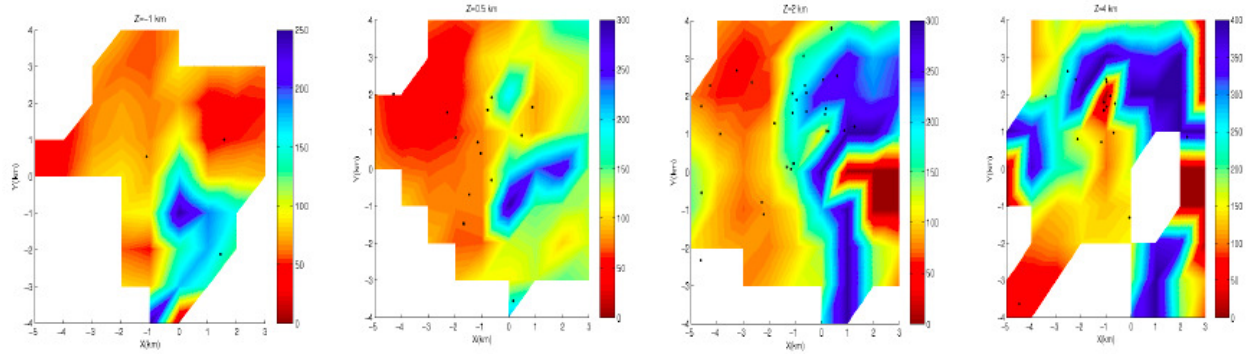

Figure 28. The horizontal slices of the Qp model at difference depths.

(5) ***Shear wave splitting analysis of the local seismic data***

We used the shear wave splitting analysis (SWS) method to analyze the data collected from our local network. The cross-correlation (CC) method (e.g. Fukao 1984), the covariance matrix (CM) method (e.g. Silver & Chan 1991), and the aspect ratio (AR) method (Shih et al. 1989) are three automated methods commonly used in SWS analysis. They can be viewed as eigenvalue-based measures of linearity of particle motion (Silver & Chan 1991). In an ideal situation, all these methods should give identical results. For real data, the analyzed results may vary with the employed method.

In the CC method, the two horizontal seismograms are rotated in the horizontal plane at a 1^o increment of azimuth α from 0^o to 180^o. For each azimuth, the cross-correlation coefficient (CCC) between the two orthogonal seismograms is calculated for a range of time delays (TDs) τ in a selected time window. When the absolute value of the CCC $c(\alpha,\tau)$ reaches a maximum, the corresponding values of α and τ are chosen as the PD of the fast shear wave (FSW) and the time delay of the slow shear wave (SSW), respectively. The underlying assumption of the CC method is that the fast and slow horizontal components have similar waveforms. However, for local earthquake seismograms, the fast and slow horizontal components may or may not display similar waveforms, as the polarizations respond differently to the structure between source and receiver (Aster *et al.* 1991; Liu *et al.* 1997, Liu *et al.* 2005b). Similar to the CC method, the CM method finds the SWS parameters based on minimizing the smaller eigenvalue of a 2 x 2 covariance matrix constructed from the horizontal-component seismograms. The AR method maximizes the ratio between the larger and smaller eigenvalues of the covariance matrix to determine the fast polarization direction. The ideal window for calculating the AR value should start at the onset of the FSW and end right before the arrival of the SSW. An optimal window is obtained by testing various window lengths. Once the PD is resolved, the TD is estimated by cross-correlating the FSW with the SSW. The AR method excels in estimating the PD when the TD of the SSW is large (e.g. > 0.1 sec) and signal to noise ratio is high, regardless of the similarity between the fast and slow components (Liu *et al.* 2004). However, we found that the CC method gives much more robust results than the AR method for our data set, in which the S phases are usually contaminated with the coda of the P phases and the TDs between the fast and slow shear waves are usually not very large.

Figure 29 illustrates the SWS analysis process on an earthquake recorded by station ME02A using the CC method. The original short period 3-component seismograms are given in Fig. 1a. The shaded areas indicate the time window for SWS analysis. A contour plot of the CCC values is shown in Figure 29b. The maximum CCC value is indicated by the cross and its corresponding azimuth and time delay give the PD (here 4^o) and the TD (here 0.06 sec). Fig. 1c is a slice through Figure 1b at the determined PD. Fig. 1d shows the horizontal component waveforms rotated into the determined PDs of the FSW and the SSW. Fig. 1e shows the horizontal particle motion of the original seismograms. As a check, we advance the SSW with the estimated TD and show the resulting horizontal particle motion and the shifted seismograms in Figures 29f and 29g, respectively. The linear particle motion in Figure 29f and well-matched seismograms in Figs 29g indicate that the above measurement is valid.

We applied the shear-wave splitting analysis method to around 200 seismic events collected. Figure 30 shows the average delay times and polarization directions. It can be seen that with the increase of event depths the delay times do not tend to increase. This indicates that the anisotropy is mostly confined to the shallow depths. The average polarization directions at

different stations are consistent, pointing to the NNE direction, indicating that the major fault/fracture direction may be along the NNE direction if the anisotropy is caused by fault frabric.

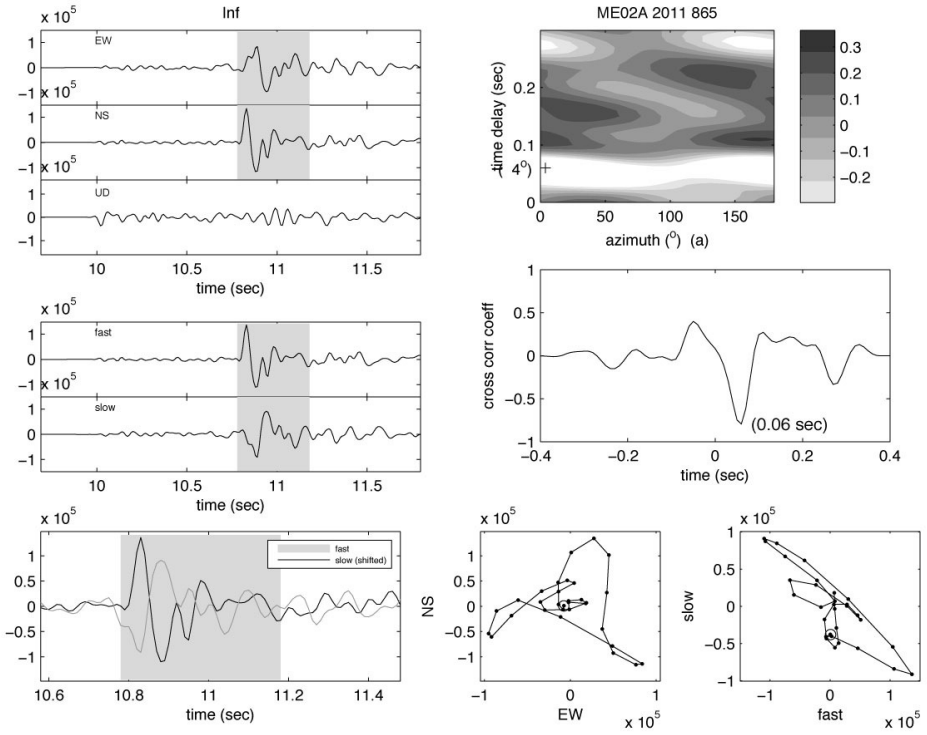

Figure 29. An example of SWS analysis with the CC method. (a) Original three-component seismograms. (b) A contour plot of the CCC values. The maximum CCC value is indicated by the cross at PD = 4° and TD = 0.06 sec. (c) A slice of (b) at the measured PD. (d) Seismograms rotated to the estimated fast and slow PDs. (e) The horizontal particle motion of the original seismograms. (f) The horizontal particle motion of the fast and slow components shifted with the measured TD. (g) Waveforms of the fast and slow components shifted with the measured TD.

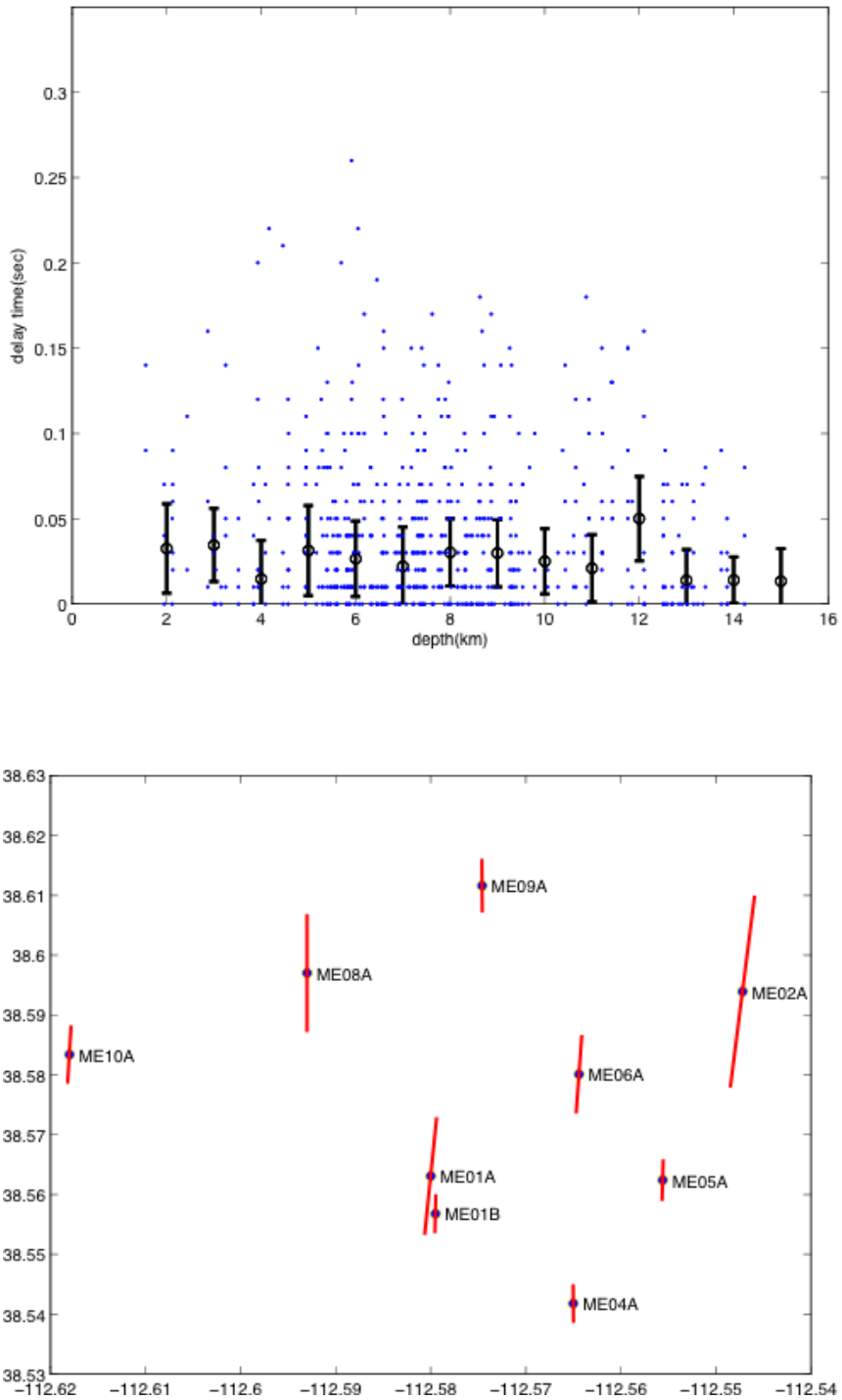

Figure 30. Average delay times (top) and the average fast polarization directions from shear wave-splitting analysis.

(6) Determining focal mechanisms using the waveform fitting

To study the local stress region and understand the tectonic settings, we invert for the source mechanisms of (*to add more events*) events by matching the waveforms, the first P-arrival polarities and the ratios between shear waves and compressional waves (Li et al., 2011). The comparison between the observed and synthetic waveforms is shown in Figure 31.

Figure 32 shows the locations of microseismic events and the source mechanisms of selected events. The distribution of hypocenters suggests two faulting systems: one trends in the NNE direction, and the conjugate one trends in the NW direction. Among the events inverted for source mechanisms, we found the normal faulting events have strikes in NNE direction, and the events with strike slip mechanism have strikes either parallel with the NNE trending faults or their conjugate ones. Assuming the maximum horizontal stress (SH_{max}) is parallel with the strike of the normal faulting events, and bisects the two fault planes of the strike-slip events (Zoback, 2007), the inverted source mechanism suggests a NNE oriented maximum horizontal stress regime, which is consistent with our current understanding of the tectonics in this region (Nafi says this area is under W-E tensional stress, which means maximum compressional stress should be in the N-E or NNE direction in general).

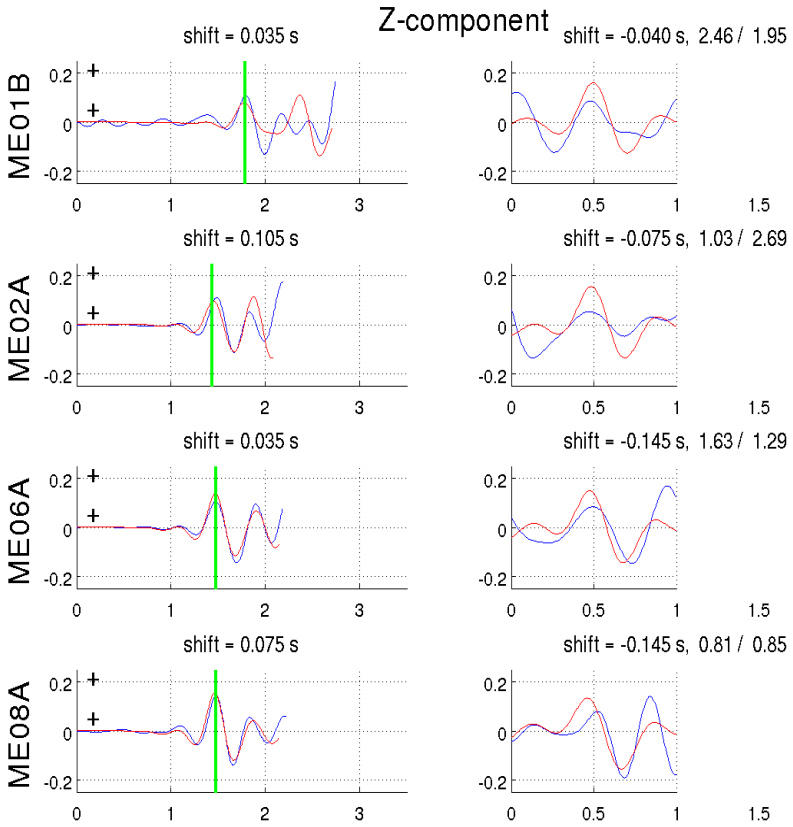

Figure 31. Comparisons between modeled waveforms (red) and observed data (blue) at 4 stations with perturbed velocity model. From top to bottom, waveforms from the vertical components at stations 1 through 4, respectively, are shown. The left column shows P-waves and right column shows S-waves. In the left column, the "+" or "-" signs indicate the first arrival polarities of P-waves in the observed data and those in the modeled data, respectively. In the right column, the number to the left of the slash denotes the S/P amplitude ratio for the synthetic data, and the number to the right of the slash denotes the ratio for the modeled waveform.

Figure 32. Locations of microseismic events and inverted source mechanisms for selected events. The blue triangles indicate the surface stations, and the blue dots indicate the location of the induced microseismic events. The stars indicate the location of the selected events of which we inverted for the source mechanisms.

Discussions and Conclusions

To characterize the geothermal system underneath the Cove Fort geothermal site, we first collected the regional data including gravity, seismic, and heat flow. Through a separate seismic inversion and the joint inversion, we derived a regional velocity model for the Utah area. The velocity model clearly indicates that underneath the Cove Fort geothermal site there is a strong low velocity anomaly. By combining high heat flow and low gravity anomaly in the region, we can derive that there is a hot body beneath the Cove Fort geothermal site. Below 7 km of the mean sea level, we assume the high temperatures cause the low velocity anomaly. Through the relationship of the velocity variation versus temperature, we can derive the temperature anomaly with respect to the normal temperature. On average, the temperatures in the hot body are about 150 ˚C – 200 ˚C hotter than the surrounding rock.

For the regional velocity model, it lacks the necessary resolution to characterize the detailed structure at the shallow depths. The local seismic data collected from a 10-station seismic network complements the lack of resolution for the regional model at shallow depths. Using about 200 seismic events, we determined the 3D velocity models of the shallow region around the Cove Fort. It shows that the major target for geothermal development is a high velocity body. We interpret it due to the monzonite, an intrusive igneous rock. The attenuation tomography results also showed that the high velocity body corresponds to the high Q anomaly.

To determine the fracture direction, we used the shear wave splitting analysis and the focal mechanism analysis. Both analyses showed that in the Cove Fort area, the fractures mainly point to NNE direction.

The model used in this study is an effective tool for approximating the temperature and spatial extent of geothermal reservoirs. With the addition of compositional and structural details, the model has the potential to provide more detailed information on temperature, heat sources and fluid transfer in geothermal reservoirs, information that could prove invaluable for industrial exploitation of the resource.

References

Armstrong, R.L. (1968). Sevier Orogenic Belt in Nevada and Utah, *GSA Bulletin,* **79,** 4, 429-458.

Benson, T.R., 2009. Geophysical models for evaluating the feasibility of enhanced geothermal systems in New Hampshire. B.A. Thesis, Department of Earth and Planetary Sciences, Harvard University.

Benz, H.M., R.B. Smith and W.D. Mooney (1990). Crustal Structure of the Northwestern Basin and Range Province from the 1986 Program for Array Seismic Studies of the Continental Lithosphere Seismic Experiment, *Journal of Geophysical Research* **95**, B13, 823-842.

Best, M.G., E.H. McKee and P.E. Damon (1980). Space-time composition patterns of late Cenozoic mafic volcanism, southwestern Utah and surrounding areas, *American Journal of Science,* **280**, 1035-1050.

Blackwell, D. D., Richards, M., 2004. Geothermal Map of North America. American Assoc. Petroleum Geologist (AAPG), 1 sheet, scale 1:6,500,000.

Callaghan, E. (1973). Mineral resource potential of Piute County, Utah and adjoining area, *Bulletin - Utah Geological and Mineral Survey*, **102**, 135 pp.

Crosby, G.W. (1959). Geology of the south Pavant Range, Millard and Sevier counties, Utah, *Brigham Young University,* M.S. Thesis, 59 pp.

DeCelles, P.G., Coogan, J.C., 2006. Regional structure and kinematic history of the Sevier fold-and-thrust belt, central Utah. Geol. Soc. Am. Bull. 118, 841-864.

Dickinson, W.R., 2006, Geotectonic evolution of the Great Basin. Geosphere 2, 7, 353-368.

Fleck, R.J., J.J. Anderson and P.D. Rowley (1975). Chronology of mid-Tertiary volcanism in High Plateaus region of Utah, *Geological Society of America Special Paper,* **160**, 53-61.

Foulger, G. R., C.C. Grant, A. Ross, and B.R. Julian (1997). Industrially induced changes in Earth structure at The Geysers geothermal area, California, Geophys. Res. Lett., **24**, 135 – 137.

Gunasekera, R.C., G.R. Foulger, and B.R. Julian (2003). Reservoir depletion at The Geysers geothermal area, California, shown by four-dimensional seismic tomography, J. Geophys. Res., **108**, 2134, doi:10.1029/2001JB000638.

Haenel, R., L. Rybach and L. Stegena (1988). Fundamentals of Geothermics, *Handbook of Terrestrial Heat-Flow Density Determination,* Kluwer Academic Publishers, Netherlands, p. 9-57.

Henrikson, A. and D.S. Chapman (2002). Terrestrial Heat Flow in Utah, *University of Utah*

Department of Geology and Geophysics.

Hughes, D.S., Maurette, C.G., 1956. Variation of elastic wave properties in granites with pressure and temperature. Geophysics 21, 2, 277-284.

Hughes, D.S.,Maurette, C.G., 1957. Variation of elastic wave properties in basic igneous rocks with pressure and temperature. Geophysics 22, 1, 23-31.

Julian, B.R., G.R. Foulger (2009). Time-dependent seismic tomography of geothermal systems , Proceedings of Thirty-Fourth Workshop on Geothermal Reservoir Engineering, Stanford University, Stanford, California, February 9-11, 2009, SGP-TR-187.

McKee, E., 1971. Tertiary igneous chronology of the Great Basin of Western United States; implications for tectonic models. Geol. Soc. Am. Bull. 82, 3497-3501.

Moore, J.N. and S.M. Samberg (1979). Geology of the Cove Fort-Sulphurdale KGRA, *Univ. Utah Res. Inst., Earth Sci. Lab. Report,* **ESL-18**, 44 pp.

Nelson, S.T., Harris, R.A., Kowallis, B.J., Dorais, M., Constenius, K.N., Heizler, M., Bernett, D., 2009. The long-term burial and exhumation history of basement blocks in the footwall of the Wasatch fault, Utah. Rocky Mtn. Geol. 44, 2, 103-119.

Parsons, T., 1995. The Basin and Range Province, in: Olsen, K.H. (Ed.), Developments in Geotectonics 25: Continental Rifts: Evolution, Structure, Tectonics. Elsevier, Amsterdam, pp. 277-324.

Podvin, P. and I. Lecomte (1991). Finite difference computation of traveltimes in very contrasted velocity models; a massively parallel approach and its associated tools, *Geophysical Journal International*, **105**, 1, 271-284.

Ross, A., G.R. Foulger and B.R. Julian (1999). Source processes of industrially-induced earthquakes at The Geysers geothermal area, California, Geophysics, **64**, 1877–1889.

Ross, H.P., J.N. Moore and O.D. Christensen (1982). The Cove Fort-Sulphurdale KGRA; a geologic and geophysical case study, *Univ. Utah Res. Inst., Earth Sci. Lab. Report,* **ESL-90**, 47 pp.

Ross, H.P. and J.N. Moore (1985). Geophysical investigations of the Cove Fort-Sulphurdale geothermal system, Utah, *Geothermics*, **50**, 11, 1732-1745.

Rowley, P.D., C.G. Cunningham, J.J. Anderson and T.A. Steven (1979). Geologic map of the Marysvale SW Quadrangle, Piute County, Utah, *Miscellaneous Field Studies Map - U. S. Geological Survey*, **MF- 1116**.

Spencer, J.E., 1996. Uplift of the Colorado Plateau due to lithosphere attenuation during Laramide low-angle subduction. J. Geophys. Res. 101, 13, 595-609.

Steven, T.A., C.G. Cunningham, C.W. Naeser and H.H. Menhert (1979). Revised stratigraphy and radiometric ages of volcanic rocks and mineral deposits in the Marysvale area, West-central Utah, *U. S. Geological Survey Bulletin*, **B-1469**, 40 pp.

Steven, T.A. and C.G. Cunningham (1979). Clinoptilolite resources in the Tushar Mountains, West-central Utah, *Open-File Report - U. S. Geological Survey*, **OF 79-535**, 22 pp.

Steven, T.A. and H.T. Morris (1981). Preliminary geologic map of the Cove Fort Quadrangle, West-central Utah, O*pen-File Report - U. S. Geological Survey*, **OF 81-1093**, 15 pp.

Steven, T.A. and H.T. Morris (1983). Geologic map of the Cove Fort Quadrangle, west-central Utah, *Miscellaneous Investigations Series - U. S. Geological Survey*, **I-1481**.

Wannamaker, P.E., D.P. Hasterok, J.M. Johnston, J.A. Stodt and others (2008). Lithospheric dismemberment and magmatic processes of the Great Basin-Colorado Plateau transition, Utah, implied from magnetotellurics, *Geochemistry, Geophysics, Geosystems*, **9**, 5, 38 pp.

Yang, Y., M. H. Ritzwoller, F. - C. Lin, M. P. Moschetti, and N. M. Shapiro (2008), Structure of the crust and uppermost mantle beneath the western United States revealed by ambient noise and earthquake tomography, *J. Geophys. Res.*, **113**, B12310, doi:10.1029/2008JB005833.

Zhang, H. and C.H. Thurber (2003). Double-difference tomography; the method and its application to the Hayward Fault, California, *Bulletin of the Seismological Society of America*, **93**, 5, 1875-1889.